

Estimating Noise Floor in Sentinel-1 Images with Linear Programming and Least Squares

Peter Q. Lee, *Student Member, IEEE*, Linlin Xu, *Member, IEEE*, and David A. Clausi, *Senior Member, IEEE*

Abstract—Sentinel-1 is a synthetic aperture radar platform that provides free and open source images of the Earth. A product type of Sentinel-1 is Ground Range Detected (GRD), which records intensity while discarding phase information from the radar backscatter. Especially in cross-polarized GRD images, there are noticeable intensity changes throughout the image that are caused by amplifying the noise floor of the signal, which varies due to non-uniform radiation pattern of the satellite’s antenna. While Sentinel-1 has Instrument Processing Facility (IPF) software to estimate the noise floor, even in the newer versions (3.1 or above) of the IPF software there are still instances where the estimates provided do not fit to the actual noise floor in the image, which is particularly noticeable in transitions between adjacent subswaths.

In this work we propose a method that reduces the impact of the varying noise-floor throughout the image. The method models the intensity of the noise floor to be a power function of the radiation pattern power. The method divides the swath into several sections depending on the location of the local minimum and maximum of the radiation pattern power with respect to the range. The parameter estimation is portrayed as a geometric programming problem that is transformed into a linear programming problem by logarithmic transformation. Affine offsets are computed for each subswath by a weighted least squares approach. Vast improvement is found on extra-wide (EW) and Interferometric Wide (IW) Sentinel-1 modes over cross-polarized images. Code implementation is available at https://github.com/PeterQLee/sentinel1_denoise_rs.

Index Terms—Sentinel-1, SAR, noise floor, denoising, additive noise, linear programming

I. INTRODUCTION

¹ Synthetic aperture radar (SAR) is a method of remote sensing that uses backscatter from emitted radar pulses to infer physical characteristics about the surface. Sentinel-1 is a mission by the European Space Agency (ESA) that uses two satellites (Sentinel-1A and Sentinel-1B) to provide a free and open source of SAR images of the planet. Consequently, Sentinel-1 remains an important resource for remote sensing practitioners.

In every Sentinel-1 product there are one or two image files that represent the recorded backscatter, which we will call the unprocessed images, in addition to several other files containing metadata. One issue that is apparent in unprocessed images are the noisy intensity patterns that disrupt the appearance of the desired backscatter intensity, which are sometimes described as additive noise, noise equivalent sigma zero, or as scalloping and banding patterns. Throughout this paper these

noise patterns will be described as the noise floor of the image, which is the total sum of noise sources within a signal measurement. Throughout its lifespan, Sentinel-1 has had multiple iterations of its Instrument Processing Facility (IPF) software, which provides a method of estimating and subtracting the noise floor from the image in order to normalize the intensity within the image. In IPF 2.9, azimuth vectors were added to compensate for the scalloping patterns that occur along the azimuth [1]. In IPF 3.1 further improvements were made to improve the consistency of the noise floor among different subswaths [1]. In early versions of the IPF, remote sensing practitioners had difficulty compensating for the varying noise floor, particularly in cross-polarized images [2], [3], [4], [5]. While more recent versions have improved this, issues still remain. The recent article by [6] evaluated the calibration of Sentinel-1 images finding that calibration can suffer particularly in scenarios with lower backscatter. In addition to radiometric differences between the two satellites, it was also found that the look angle was a factor for discrepancies in intensity.

The types of images most affected by the noise floor issue are cross-polarized images over maritime regions, due to the low backscatter of ice and water. Consequently, noise floor removal is critical for applications that require uniform and consistent measurements throughout the image. One such application is sea ice analysis, where the backscatter is used to determine the physical qualities of the ice [2], [5]. Wind speed analysis also relies on cross-polarized images, with the literature showing that wind speed algorithms are adversely affected by the noise floor patterns in Sentinel-1 images [7], [8]. Therefore, ensuring homogeneous intensity throughout cross-polarized images could greatly improve visual interpretation and the performance of the models applied for these tasks.

There are a limited number of methods in the literature that attempt to compensate for the noise floor in Sentinel-1 images. In the work by [4], a methodology was proposed that rescales the default ESA noise floor in an affine manner for each subswath. Our previous work [9] built onto the work of [4] by formulating a method to dynamically estimate parameters of the noise floor specific to each image. Specifically, a least squares approach was used to estimate linear scaling parameters for each of the different subswaths such that applying this re-scaled noise floor results in a more consistent intensity profile throughout the image. However, as noted [9], the noise floor is sometimes misfit in a non-linear manner that makes it not possible to choose a linear scaling parameter that satisfies all sections within a subswath. Sun and Li [10] took a similar approach of estimating linear scaling parameters based on the variance of adjacent subswaths. The authors also attempted

¹An initial version of this work appeared in the conference IEEE International Geoscience & Remote Sensing Symposium (IGARSS 2020) under the title of Recalibrating Sentinel-1 Additive Noise-Gain with Linear Programming. The initial component of this work was a part of P.L.’s Masters thesis.

to compensate for the textural patterns that are caused by the noise-floor effect, a topic also pursued by Park *et al.* [11], although it should be noted that the scope of this paper is firmly based on the issue of the additive bias of the noise floor rather than the textural issues.

In this work, we attempt to compensate for this non-linear misfit of the noise floor in the subswaths. We observe that the radiation pattern of the platform matches the scale of the true noise floor much better than the ESA noise floor. We propose a novel model of the noise floor to be a power function of the platform’s radiation pattern, whose parameters are estimated by solving a geometric program, that is converted to a linear program in the log transformed domain. To ensure compatibility between adjacent subswaths, offsets for each subswath are computed using a weighted least squares formula to compensate for the gamma distribution of backscatter. This work makes refinements of our initial research presented in the conference IGARSS 2020 [12] by modifying the model to estimate different power functions based on range splits (see Section III-A), improving the offset estimation with gamma variance weighting (see Section III-B), providing more details and motivations behind the algorithms, and providing a more complete analysis of the model by considering IW mode images, more diverse EW mode images, a simulation experiment (Section IV-A), an experiment analyzing the effects on bias (Section IV-C), and an extended discussion (Section V).

We evaluate our method with three experiments. The first experiment evaluates the performance of the proposed method within a simulated experiment on a selection of RADARSAT-2 images. The second experiment evaluates the method on a selection of Sentinel-1 images, using version IPF v3.1+, in both EW and IW mode, whose quantitative performance is determined based on the characteristics of open water in the images. The third experiment determines the difference in radiometric bias compared to the default ESA method. Overall, the first two experiments showed that the proposed method is able to substantially improve the image quality under different conditions, particularly in its ability to correct for the non-linear misfit in the images. The third experiment indicated that the proposed method results in a different radiometric bias than the baseline ESA method. However, it is unclear whether the radiometric bias change is an error, as there are some examples where the ESA method loses significant features in images. Therefore, we recommend further studies comparing known materials to the backscatter for calibration purposes.

II. BACKGROUND

To understand the problem of estimating the noise floor, we first provide an abridged overview of how the Sentinel-1 SAR platform operates in GRD mode, which records backscatter intensity and discards phase information (c.f. [13]). The satellites emit radar pulses towards the surface of the planet, measure the backscatter signal produced, and create images based on these measurements. The backscatter intensity depends on factors of the sensor (e.g., antenna radiation power, wavelength, and look angle) and the environment (e.g., surface roughness and

dielectric properties). If a hypothetical isotropic antenna were used, the antenna’s radiation power (P) would be identical in all relevant directions and thus could be considered as a constant. However, due to the limits of manufacturing, the radiation pattern of Sentinel-1 antennas are non-isotropic and vary depending on the look angle. To compensate for the varying radiation pattern, the measured signals must be amplified differently according to the azimuth and elevation angle to ensure that the backscatter measurements are comparable throughout the image. An impact of this amplification is that the thermal noise floor, which is the lowest possible measured signal caused by the sum of noise sources (e.g., within the circuitry of the satellite) [14], is also amplified differently according to look angle. This results in non-stationary noise floor patterns throughout such images because regions that are acquired with lower radiation power have an amplified noise floor with higher intensity and regions that are acquired with higher radiation power have an amplified noise floor with lower intensity. In Sentinel-1 this has been called additive noise or noise equivalent sigma zero (NESZ) and is commonly associated with banding and scalloping patterns [15], [16].

The two Sentinel-1 modes this paper considers are Extra-wide (EW) and Interferometric Wide (IW) modes, which have the option to produce GRD types of images. These sensor modes use Terrain Observation with Progressive Scans SAR (TOPSAR) to scan in a compromise between resolution and surface area covered [17]. TOPSAR works by breaking an area into different subswaths defined in the range direction. During orbit, it measures all subswaths concurrently by sequentially emitting bursts rotated towards different elevation angles that correspond to the different subswaths. Due to the design of the antenna, the radiation pattern is unique for each subswath. EW mode has five subswaths and is typically applied to ocean regions with its first subswath, EW1, having a very high magnitude noise floor with a multimodal pattern, while the remaining four subswaths, EW2, EW3, EW4, and EW5 have U-shaped patterns. IW mode has three subswaths, IW1, IW2, and IW3, all of which have U-shaped patterns. For both of these sensor modes, the higher numbered subswaths will typically be generated with higher radiation power than the earlier subswaths. The unprocessed images have significant changes of intensity due to the varying noise floor. The changes are particularly abrupt at boundaries between subswaths, since the radiation patterns used are discontinuous due to the subswath merging. Fig. 1 shows examples and the relationship between the estimated noise floor and the antenna radiation power.

Note a couple of conventions in this paper. In Sentinel-1 products measurements and noise-floor estimate are typically specified in pixel coordinates that may be exchanged with the appropriate azimuth and ground/slant range angles with provided lookup tables. Because the noise floor removal is typically done on the image level, the azimuth and range will be specified in row and column coordinates throughout this paper. Also, at the noise floor removal stage values are still specified in terms of Digital Numbers (DN). This is prior to when the DN converted to backscatter quantities (e.g., $\sigma_0, \beta_0, \gamma$). Because our pipeline is firmly entrenched in the noise floor removal stage, this paper will primarily report

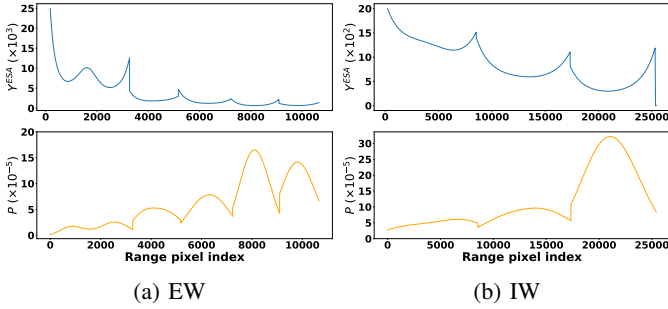


Fig. 1: Plots of the estimated noise floor (top) and the antenna radiation pattern power (bottom) along the range direction for both EW and IW images (unit-less). Their values show an inverse relationship. Both the ESA noise floor and antenna radiation power values were derived from XML files from the Sentinel-1 products.

results in terms of Digital Numbers.

The ESA provides noise-calibration *extensible markup language* (XML) files that estimate the noise floor $Y_{ESA} = n_{az}n_{rc}$, with n_{az} and n_{ra} being the azimuth and range noise vectors, so that subtracting the original image and the noise floor will result in a more consistent intensity profile throughout the image. However, as shown in previous work [9], these estimations have issues fitting to the images. While linear rescaling methods improve on this [4], [9], a critical issue that remains is that there is non-linear mis-scaling within each subswath [9]. For instance, Fig. 2a plots the ESA noise floor and the observed measurement of open water respect to the range that demonstrates an example where the noise floor is misfit in a non-linear manner. Linear rescaling will not fix this because one side of the subswath is under-compensated, while the other is over-compensated.

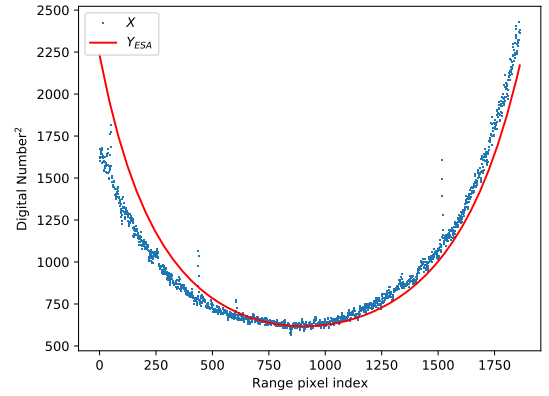
The observation that motivates this work is that in the log-log domain a piece-wise linear function can be used to describe the true noise floor with respect to the antenna pattern. Fig. 2b demonstrates this by showing an example of the log transformed antenna pattern with respect to log transformed measurements over a section of open water, which is a good approximation of the true noise floor. The figure also shows that there is also a piece-wise relationship between the ESA noise floor and the measurements, an aspect that will be discussed further in Section III-A.

III. METHODS

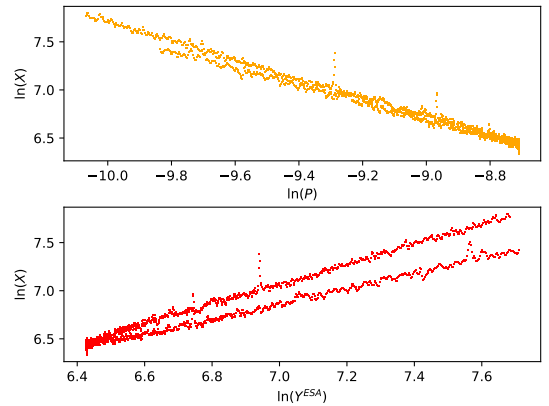
Given our observations above, we wish to model noise floor, Y , as a power function of the antenna radiation pattern

$$Y = e^b P^m Y_{azimuth} + o. \quad (1)$$

with the goal of removing the noise floor through subtraction ($X - Y$). In terms of **measured variables** Y_{ESA} as the default noise floor provided by ESA, $Y_{azimuth}$ as the azimuth noise vectors, X as the raw measurements, and P as the elevation antenna radiation pattern. In addition, we have **optimization parameters** that are estimated from the data from each scene: m , b , and o . These parameters serve different purposes. The



(a) Figure shows clear misfit between the default noise floor (Y_{ESA}) and the measurement over open water (X), a material that has low backscatter in cross-pol and therefore a good estimate of the true noise floor. Note that the left side of the subswath is over-compensated, while the right side is not. This implies that there is no choice of linear scale will rescale the noise floor correctly because one side of the subswath will always remain over- or under-compensated.



(b) Figure showing a log-log plot comparing measurement intensity ($\ln(X)$) to the antenna pattern power ($\ln(P)$) and the ESA noise floor ($\ln(Y_{ESA})$) respectively. Both of these trends reveal a piece-wise linear relationship in the log-log domain, showing a disjoint spatial relationship between the actual noise floor and model estimates.

Fig. 2: Non-linear misfit in a homogeneous section of EW4 (S1B_EW_GRDM_1SDH_20200111T211332_20200111T211432_019774_02563C_2069).

power function parameters, m and b , are used adapt to the overall shape of the noise floor within different sections of the subswath. The offset parameter, o , is used to correct for affine bias that may occur between the subswaths. Values for P are derived from the *antennaPattern* fields in the XML files that are included in the Sentinel-1 products, using the *geoLocationGrid* lookup tables to convert elevation angles to range coordinates. Critically, the unitless values from *antennaPattern* were divided by an arbitrarily large number that was greater than all pattern measurements (we chose $e^{43.3}$) for numerical stability purposes. The measurements, X , are taken from the image files in the product, with pixel values squared to convert to intensity. As the power function $e^b P^m$ only models the noise floor with respect to the range, we multiply it with the azimuth component of the ESA noise-calibration XML files, $Y_{azimuth}$, to compensate for scallop-

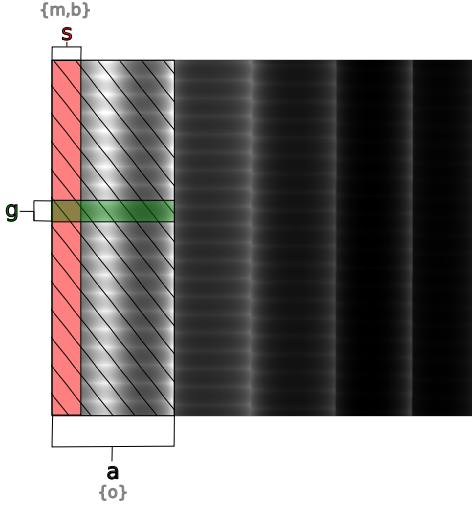


Fig. 3: Sections of an EW image divided by subswath a (hatched), bursts g (green), and range divisions s (light red). The parameter o is different for each subswath and the parameters m and b are different for each range split, as labelled in gray braces.

ing. The model (1) differs significantly from other solutions because the power function model allows the curvature of the profile to be adapted by adjusting the m parameter, in contrast to alternative linear rescaling methods. The proposed model has increased parametric complexity compared to the linear models as a consequence of generating noise floor profiles more effectively.

The images are divided into several **regions**, being the subswaths (a), range splits (s), and bursts (g) as depicted in Fig. 3, that will play a roll in how the parameters are estimated. While a is determined by the TOPSAR scanning mode, we define s as the division of the subswath along the range between the local minimum or maximum in P . Also, g corresponds to the sections TOPSAR captures along the azimuth within a radar pulse, that can be observed by the scalloping pattern along the azimuth. The power function parameters m and b are estimated in context of a geometric programming problem that is converted to a linear program and take different values for each subswath a and range split s . As will be discussed in further detail in Section III-A, the optimization attempts to take the lower bound of the aggregate values of X and P over all bursts for each subswath in range split (i.e., $g \in a \cap s$). The parameter o is found for each subswath a and is estimated by a weighted least squares. The objective of this approach is to minimize the affine offsets between the adjacent subswaths in the intermediate denoising result, \tilde{X} , of subtracting the power function, as described in Section III-B. A summary of the entire algorithm is given in Algorithm 1.

A. Power function

The idea behind estimating the parameters of the power function is that the model should act as a tight lower bound

Algorithm 1: Main procedure for noise floor estimation and subtraction in SAR image.

```

1 for each subswath  $a \in \mathcal{A}$  do
2   for each split  $s \in a$  do
3     Construct  $\mathcal{G}_{a,s}$  by Algorithm 2 // Get data
      points for lin. prog.
4     Compute parameters  $m, b$  by solving (4)
      // Solve lin. prog.
      /* With the base parameters solved, smooth
        out the function between */
      /* range splits with linear interpolation
        for each subswath. */
5   for each split  $s \in a$  do
6     Determine parameter values between the
      adjacent range split using Algorithm 3;
7     Compute  $\tilde{X}$  within  $a$  and  $s$  by computing (5)
      // Compute the partial denoised
      result, without offsets
8 Compute  $o$  by solving (6), using  $\tilde{X}$ ;
9 Compute noise floor (1) and denoise by computing
 $X - Y$ ;

```

on the measurements (X). To this end, the problem is shaped into the following geometric program

$$\begin{aligned} & \max_{m,b} e^b \Gamma^m(P, X) \\ & \text{such that } e^b P_i^m \leq X_i, \end{aligned} \quad (2)$$

with the assumption that P and X vary along the range, with P_i and X_i being observed pairs of radiation power and measurement points from the data. The intuition behind using constrained optimization to estimate the parameters is that the noise floor has the fundamental property of being the minimum measurable signal. Constrained optimization offers a way to find a lower bound of the noise floor function based on the observed measurements. To this end, the inequality constraints ensure that the parameters m, b that are estimated result in (1) being a lower bound of the measurements (X). From a typical optimization perspective, the objective function may seem unusual, as one would typically attempt to choose m, b to minimize the distance between measured points and the power function. However, in our case we want to specify tightness to the lower bound of points; minimizing the difference between points would be counter productive because the backscatter intensity interfere with this estimation. Consequently, approaches like least squares regression would not result in a viable noise floor. Therefore, the objective function $e^b \Gamma^m(P, X)$ is used to maximize the position along a moment of the curve, and allowing the inequality constraints to bound it underneath the measurements. The scalar $\Gamma(P, X)$ is chosen to utilize all available pairs of points (P and X) to arrive at an appropriate moment, which we abstain from defining until we convert (2) into a linear program.

The approach of applying log transformations to geometric programs is a prominent strategy in geometric programming in

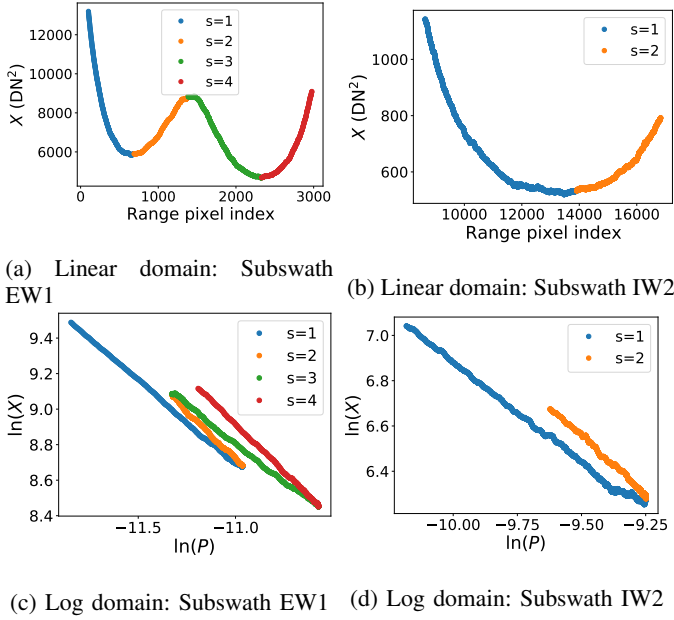


Fig. 4: Top figures show the range splits, based on the local-minima and local-maxima of the antenna pattern, corresponding to measurements in the linear domain. Bottom plots show log-log graphs of the antenna pattern versus the measured intensity. The range splits are divided in terms of colour, clearly showing that there is a linear trend that changes each time a local min/local max is passed. EW plots come from S1B_EW_GRDM_1SDH_20200112T183748_20200112T183848_019787_02569C_3399 and IW plots come from S1B_IW_GRDH_1SDV_20190908T232059_20190908T232128_017953_021CC5_7FCE.

order to make original problem easier to solve [18]. The special case of the power function is convenient as it transforms directly to a linear function

$$\ln(e^b P^m) \equiv m \ln(P) + b \equiv mp + b. \quad (3)$$

Given our observations in Section II pertaining to the linearity of the true noise floor in the log-log domain, it is logical to transform the objective function to be a linear function. Optimizing parameters of a linear objective function with respect to a set of linear inequalities is the definition of a linear program [19]. This is convenient as linear programs are a well known class of problems with many applicable algorithms available for use.

We aim to model several different functions contingent to the different subswaths (a) and range splits (s) discussed above. We observe that on open water regions the linear trend changes slope at different range sections of the subswath, which we call range splits. These changes appear at local minimum and maximum of the radiation pattern power. An example of this is shown in Fig. 4. Therefore, separate power functions are modelled for every range split s in each subswath a .

The aim for the parameter estimation problem is to tightly fit the power function to the true noise floor as it varies along the range. To use the measurements for parameter estimation, several preprocessing steps are needed. As we aim to model separate power functions for every range split s ,

we require a method to obtain potential points of the true noise floor throughout s from which to estimate the power function parameters. We denote this set of points as $G_{a,s}$, by extracting pairs of log transformed antenna pattern values and measurements (p_i, x_i) over all bursts within a and s . The overall process of constructing $G_{a,s}$ is given in Algorithm 2. The method involves extracting indices that cover the overlap between burst g and slice $s \in a$, and gathering the average measurements along the range. Further processing is done in the form of convolution with a boxcar filter of size 51 (to remove outliers). A critical step is the subtraction that occurs on line 6 using a set of values from B that represent the minimum value of noise floor free backscatter measurements for a specific burst and subswath. This is important for allowing the method to adapt to different target compositions and ensuring the lower bound that is found will represent an appropriate noise floor. Note that for the set B , we selected the minimum measurements that are produced by the ESA noise floor removal method for each burst and split. Note that if one has some alternative prior information on what the minimum backscatter should be, this could be replaced and could possibly result in a better quality lower bound and improve parameter estimation.

Algorithm 2: Construct $G_{a,s}$

- 1 Let $G_{a,s} = \{\}$;
 - 2 Let B be a set of estimates of the minimum noise floor free measurement for each burst in subswath a ;
 - 3 **for** each burst $g \in a$ **do**
 - 4 Let $\bar{X} =$ mean reduction of $X \in \{g \cap s\}$ along the azimuth axis; // obtain a 1D array of measurements with respect to the range
 - 5 Let $\mathbf{T} = \bar{X} * \text{boxcar}(51)$; // Smooth array with low pass filter
 - 6 Let $\mathbf{Q} = \mathbf{T} - B(g)$; // Subtract the minimum measured value, so that \mathbf{Q} is closer to the true noise floor
 - 7 Update $G_{a,s} \implies G_{a,s} \cup (\ln(\mathbf{Q}), \ln(\{\mathbf{P} \in s\}))$; // Concatenate the altered measurements and antenna pattern
-

The linear program takes the form of

$$\begin{aligned} & \max_{m,b} \gamma m + b \\ & \text{such that } mp_i + b \leq x_i \quad \forall (x_i, p_i) \in G_{a,s}, \\ & m \leq -0.75, \text{ and } m \geq -1.25, \end{aligned} \quad (4)$$

where m and b are optimization parameters, (x_i, p_i) are pairs of points obtained by Algorithm 2, and γ is the objective variable. Again, note that different versions of m , b , and γ are created for every pair of subswath a and split s , but are not annotated differently in the formulas for visual clarity. As mentioned previously, by estimating parameters m and b in a linear function $mp + b$ in log space is equivalent to $e^b P^m$, which is part of the proposed model of the noise floor.

Because the noise floor is the lower bound signal, linear constraints $mp_i + b \leq x_i$ are set, indicating that the noise

floor estimate cannot exceed the signal measurements. We also found it beneficial to add additional inequalities $m \leq -0.75$ and $m \geq -1.25$, since occasionally the program would result in extreme slope values that were inappropriate.

The objective $\gamma m + b$ is designed to promote a line that is close to the constraining points as possible. If one ignores the $m \leq -0.75$ and $m \geq -1.25$ constraints, mathematically the choice of γ must be between $\min(\mathbf{p})$ and $\max(\mathbf{p})$ or else the linear program has the possibility of being unbounded. More intuitively, γ could be thought of the factor controlling where the line should be most tight to the constraining points. For example, if γ is chosen as $\max(\mathbf{p})$ then the resulting line will be tight for points close to $\max(\mathbf{p})$, but looser for points close to $\min(\mathbf{p})$, and vice versa. Thus, a choice of γ should be chosen so that the resulting line is suitable for as many points as possible. While a naïve choice of γ would be the mid point of $\{p_i \in \mathcal{G}_{a,s}\}$, this would cause a bias towards lower values due to the logarithmic transformation. To account for this, an unbiased value of γ is determined by selecting the associated points $\{(x_{\min(p)}, \min(p)), (x_{\max(p)}, \max(p))\} \in \mathcal{G}_{a,s}$ in order to compute the midpoint $v = \ln\left(\frac{\exp(x_{\min(p)}) + \exp(x_{\max(p)})}{2}\right)$. The percentage scaling is put back into the log scale as $\alpha = \frac{v - x_{\min(p)}}{x_{\max(p)} - x_{\min(p)}}$. Finally, $\gamma = \max(p) - \alpha(\max(p) - \min(p))$.

Since (4) and all its requisite terms have been determined, there are no further major steps for estimation, as the desired parameters m and b can be easily determined by using off-the-shelf solvers. We implemented the problem by using the cvxpy library[20], [21] with the splitting conic solver [22], [23] to solve for the parameters. This process is repeated for each division of subswaths independently. For reference, Fig. 5 shows an example of the bounding line estimated from (4) aggregated over a series of non-homogeneous series of bursts.

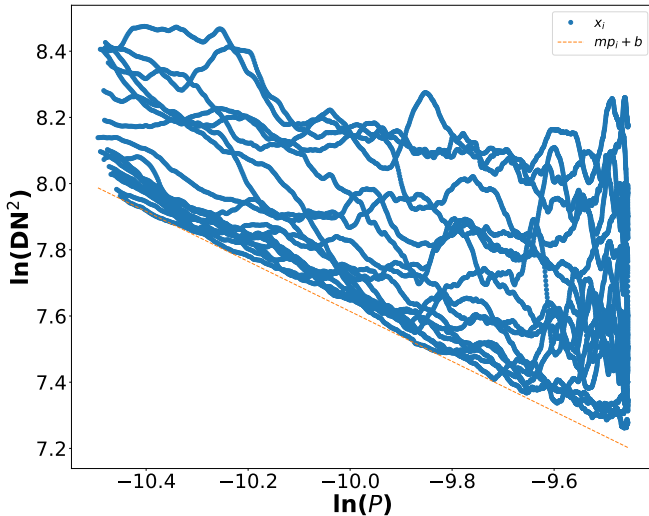


Fig. 5: Example of the bounding line estimated from the linear program using data points from aggregated non-homogeneous bursts in a range split. The processed log measurements, $x_i \in \mathcal{G}_{a,s}$, in blue are bounded by the dashed orange line, $mp_i + b$, so that all x_i are above this line. Data from SIB_EW_GRDM_ISDH_20191218T193518_20191218T193618_019423_024B12_5B75.

Another consideration of the algorithm is the transition

between different range splits. Due to the simplicity of the parameter estimation model, there is no guarantee that the linear functions estimated at range splits will intercept close to the measured points. If uncompensated, this can result in discontinuities in the estimated noise floor between adjacent range splits. To compensate for this, m and b are transitioned between range splits by means of linear interpolation between a boundary gap. This process is detailed in Algorithm 3. At this stage, we denote the partial corrected result as

$$\tilde{X} = X - e^b P^m Y_{azimuth}, \quad (5)$$

with $Y_{azimuth}$ being the azimuth noise vector taken from the ESA noise-calibration XML files, which is used to reduce the scalloping effect along the azimuth from stitching together the bursts that compose the image. These azimuth vectors have values around 1.0 - 1.2 and are designed to be multiplied by the range component of the noise floor, in this case $e^b P^m$ (note that we rescaled these azimuth vectors to be centered around 1.0). The azimuth component is not included in the optimization of m and b because it is minute compared to the variation along the range. Fig. 6 provides a visual example of how the parameters estimated in the log domain of each range split are mapped to the linear domain.

Algorithm 3: Smoothness interpolation of m and b between different range splits.

- 1 Let s_0 and s_1 be range splits in subswath a ;
 - 2 Let parameters m_0, m_1 and b_0, b_1 be associated with s_0 and s_1 ;
 - 3 Let $\mathbf{u} = [u_0, u_1] \in \mathbb{Z}$ be the discrete range indices dividing s_0 and s_1 ;
 - 4 $m(i) = (1 - \frac{i}{u_1 - u_0})m_0 + \frac{i}{u_1 - u_0}(m_1 - m_0)$ for $i \in \mathbf{u}$;
 - 5 $b(i) = (1 - \frac{i}{u_1 - u_0})b_0 + \frac{i}{u_1 - u_0}(b_1 - b_0)$ for $i \in \mathbf{u}$;
-

A final consideration regards the use of the ESA provided noise floor Y_{ESA} rather than the antenna pattern P to estimate m and b . Both Y_{ESA} and P present piecewise linear trends can could be interchanged within the algorithm; the main difference will be that m will be positive for Y_{ESA} . For Y_{ESA} , one will want to alter the boundary constraint to $0.75 \leq m \leq 1.25$. Using Y_{ESA} may provide some theoretical advantages because it considers factors that influence the noise floor in addition to the antenna pattern, such as power gain products and range spreading loss [13], although empirically we did not find there was a significant difference in samples we collected.

B. Subswath offsets

While we found that the power function would be effective at estimating the noise floor within subswaths, an issue remains in that the overall intensity between subswaths remains imbalanced from applying (5). To compensate, offsets are computed for each subswath using a weighted least squares approach. The core of the problem is to choose a vector of offset values

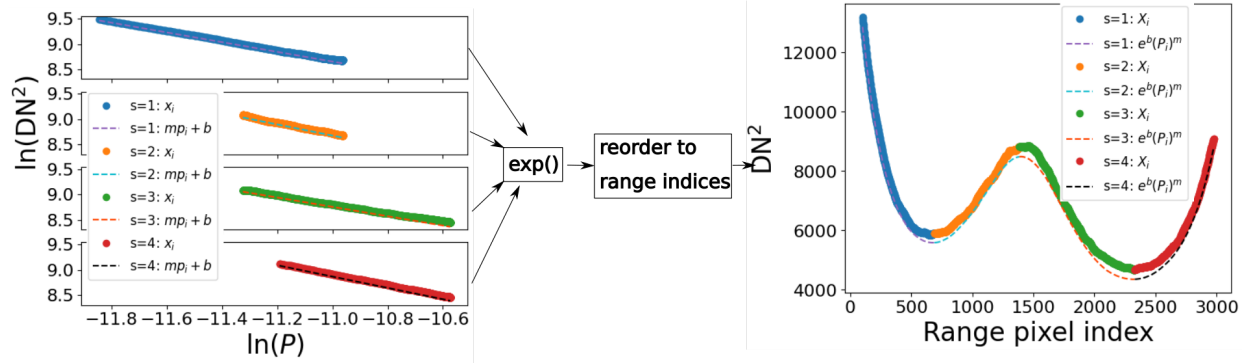


Fig. 6: Association of how the log parameters are mapped to the linear domain as the partial estimated noise floor. The figure shows the four range splits in subswath EW1 over a region of open water. The left graph shows the measurements (solid) and estimated linear function (dashed) in the log domain. After exponentiation and reordering to range indices, the right graph shows the reconstructed range measurements and noise floor estimate. Data from [S1B_EW_GRDM_ISDH_20200112T051555_20200112T051655_019779_02565A_2451](#).

so that the difference between values in adjacent subswaths is minimized. Specifically, this takes the form

$$\min_{\mathbf{o}} \sum_{a \in \mathcal{A} - \max(\mathcal{A})} \sum_{g \in \mathcal{A}} w_g (l(\tilde{X}, a, g) + o_a - (r(\tilde{X}, a, g) + o_{a+1}))^2 + \sum_{a \in \mathcal{A}} \lambda(o_a)^2, \quad (6)$$

where we take $l(\tilde{X}, a, g)$ as the average of the 30 rightmost pixels of subswath a along the azimuth lines in g , $r(\tilde{X}, a, g)$ as the average of the 30 leftmost pixels of subswath $a + 1$ along the azimuth lines in g , w_g is a burst specific weight, and \mathcal{A} is the set of subswaths in the image. In the first summation the last subswath is skipped, since there are only $N-1$ borders among N subswaths.

The selection of weights is based on the statistical distribution of SAR backscatter. SAR backscatter is distributed by the gamma distribution [24], whose variance scales with the mean of the random variables. This means that regions with higher backscatter are less reliable for estimating \mathbf{o} than regions of lower backscatter and will cause poor estimations. The variance of a gamma random variable is $E^2(X)/L$ [25], where $E(X)$ and L are the expectation of X and the shape parameter respectively (i.e., the number of looks). We incorporate this knowledge by selecting the weights to be the inverse variance of the difference of two gamma random variables

$$w_g = \frac{L}{l^2(X, a, g) + r^2(X, a, g)}. \quad (7)$$

The regularization term $\sum_a \lambda(o_a)^2$ is added to ensure that the system remains well-posed. Solving (6) is determined by solving a linear system [19].

IV. EXPERIMENTS

We implement three experiments to evaluate the impact of the proposed method (i.e., the output from Algorithm 1). The first two experiments are adapted from previous work [9] that aim to evaluate and compare the quality of the different correctional methods. The first experiment is a simulation experiment that takes 21 RADARSAT-2 images and adds

an artificial noise floor by adding (1). The second evaluates the appearance on Sentinel-1 images, measuring improvement quantitatively by the calculating the error of the measurements with respect to a linear regression over open water regions, assuming that the ideal intensity over these regions is flat. The third experiment aims to analyze the change in radiometric bias that is incurred by the proposed method on Sentinel-1 images. Where possible, we make comparisons of the proposed method to the unmodified images, the noise floor provided by ESA, which we will call Method 1: ESA S1QC IPF_v3.1+ (2020) [1], and the method from our previous work, which we refer to as Method 2: Lee *et al.*, 2020 [9]. However, Method 2 [9] was only implemented for EW images, so it was excluded for analysis concerning IW images. Note that for the quantitative measures, negative values were not clipped. However, for display purposes the values were clipped to 1% and 99% of the pixel values in each image, multilooked, and square rooted to display amplitude.

A. RADARSAT-2: Simulation

The goal of the simulation experiment is to investigate the ability to re-estimate parameters of an artificially applied noise floor, where the ground truth clean image is known. We follow the approach from our previous work [9], where we selected 21 RADARSAT-2 images over the Beaufort sea and subsequently generate and synthesize a noise floor through the power function model (1). We selected a template EW image² and a template IW image³ with similar characteristics of the RADARSAT-2 images for which to model the noise floors and intensity values.

There are several key differences in this simulation experiment compared to our previous work. First, we ran this set of experiments using both EW and IW noise floor profiles. Second, the noise floor was simulated using the power function model, rather than the noise floor originally provided by the ESA. Third, instead of selecting scaling parameters by sampling random distributions as we did in [9], we took a

²[S1B_EW_GRDM_ISDH_20200112T051555_20200112T051655_019779_02565A_2451](#)

³[S1B_IW_GRDM_ISDV_20200111T232801_20200111T232836_019776_025644_396F](#)

more conservative approach. While Method 2 [9] only had one parameter to estimate per subswath, the power function model has many more parameters (two (m, b) for each range split, plus an affine offset (o)). Randomly selecting parameters in the power function model can generate unrealistic noise floors. Instead, we found it necessary to reuse parameters that were estimated by from the experiment in Section IV-B for both of the respective template images.

Before simulating the noise on the RADARSAT-2 images, several image transformation steps were carried out to ensure that the intensity values for the RADARSAT-2 image and the Sentinel-1 image were similar. First, the pixels in the RADARSAT-2 image were squared to convert to intensity and spatially linearly interpolated to be the same size as the template. A lookup table was created to map the percentiles of the recorded intensities over all of the RADARSAT-2 images in 0.1% increments. A second lookup table was created to map the percentiles of the intensities for the template Sentinel-1 image after it was corrected by the proposed method. These two mappings were then applied to map the RADARSAT-2 intensities to the template Sentinel-1 image.

After the image transformation steps, the simulated noise floor was added onto the image using the selected parameters $X_{noise} = X_{clean} + e^{\bar{b}P^{\bar{m}}Y_{azimuth}}$, where P and $Y_{azimuth}$ were taken from the template image and \bar{b} and \bar{m} were the estimates taken from experiment in Section IV-B. As in previous work [9], we used the metrics of structural similarity index (SSIM) [26], pixel-wise normalized mean squared error (P-NRMSE), and peak signal to noise ratio (PSNR) to compare the results of the noise floor removal methods to the clean images X_{clean} , which we consider as ground truth. There were up to four different methods that would be compared, the unprocessed noisy image, Method 1 [1], the proposed method, and optionally Method 2 [9] for the EW template image.

A sample of the visual results of the simulation are shown in Fig. 7 (EW), Fig. 8 (IW), and Fig. 9, with metrics recorded in the caption. Many of the images, such as Figs. 7 and 8 appear to successfully remove the simulated noise floor as evidenced by the improved metrics, however there were a few instances, like in Fig. 9 with worse metric scores, mis-estimation in IW1, and a higher overall brightness than the clean image. The median metric values of the synthesized samples for each method are reported in Table I for both EW and IW cases. Due to the non-normal distribution of the residuals, one-tailed Wilcoxon non-parametric tests were used to test the significance of the paired difference in metrics. In terms of statistics, one-tailed Wilcoxon tests with a threshold of 0.05 were applied for each metric to determine if the proposed method was significantly better than the other methods, due to the non-normal distribution of residuals. Overall, the proposed method had better image quality than the original unprocessed image, Method 1 [1], and Method 2 [9] in terms of the metrics. The improvement was within significant levels except for Method 2 in terms of SSIM for the EW case and PSNR for Method 1 for the IW case.

B. Sentinel-1: Appearance

To evaluate our method, samples of 40 EW and 18 IW Sentinel-1A and Sentinel-1B images, with IPF version 3.1 or above, were selected to compare the proposed method to the baseline methods. For EW images, we attempted to select a sample from all five oceans. The selection of IW images was less diverse, as IW mode is not specialized towards ocean regions. Thus, the IW images were selected from a select few coastal regions in the Pacific Ocean and Hudson Bay. Some examples of these EW and IW images are shown in Figs. 10 and 11, which show the visual difference between the proposed method and the baseline methods.

Due to the unavailability of a ground truth image without noise, we could not evaluate the effectiveness of the method using conventional pixel difference measures. A characteristic we exploited for our analysis is the appearance of open water. Due to the low backscatter coefficient of calm water [6], one should expect that a region of calm water would have a relatively flat intensity profile. We then expected that significant variation along the range is a result of the changing noise floor. So if a noise floor removal method has significant variance along a region of open water, we assume that this is the result of uncompensated noise floor.

To accommodate this strategy, we selected rectangular regions from the 40 EW and 18 IW images spanning the range of the image that we deemed to be open water through visual inspection. The mean was computed along the azimuth of each rectangular regions so that points of measurements along the range were generated for each rectangle. This vector was also convolved with boxcar filter of size 151 for the values in each subswath, using valid padding, in order to remove the outliers and isolate the overall intensity changes.

The quantitative measure was derived by computing the normalized mean squared error (R-NMSE) of the processed points, as mentioned above, with respect to a best fit linear regression along the range, for each method. The median R-NMSE values and significance levels over the gathered samples are summarized in Table II. Once again, we apply Wilcoxon tests and report median values due to the non-normal distribution of the residuals. For EW, the proposed method had statistically lower R-NMSE than the unmodified image, the images produced by Method 1 [1], and those modified by using Method 2 [9]. The proposed method also had a significantly lower median for IW images, albeit the magnitude of improvement was less. While we saw an overall improvement, the magnitude of improvement varied for each image.

C. Sentinel-1: Intensity bias

One consideration to be aware of when designing noise floors is the effect of the overall intensity among subswaths after subtraction. A potential undesired outcome from modifying noise floors is raising or lowering the overall intensity of the SAR images so that the backscatter intensity does not match the expected intensity of a physical ground target, so that there is a bias of intensity away from expected radar cross section. Consequently, this experiment aims to evaluate how the total

TABLE I: Quality metric comparisons for simulation experiment. Median values are reported for each method over all simulated samples. P-values are taken from a one-tailed Wilcoxon test, comparing the metrics to the proposed method. Bold p-values indicate significance and non-bold indicates non-significance at a threshold of 0.05.

| Method | P-NRMSE | P-value | PSNR | P-value | SSIM | P-value |
|--------------|-----------------------|---|-------|---|------|---|
| EW (N=21) | | | | | | |
| Original | 3.49×10^{-1} | 2.98×10^{-5} | 19.92 | 2.98×10^{-5} | 0.43 | 2.98×10^{-5} |
| Method 1 [1] | 6.73×10^{-2} | 2.98×10^{-5} | 28.68 | 2.98×10^{-5} | 0.79 | 1.85×10^{-3} |
| Method 2 [9] | 1.88×10^{-2} | 4.51×10^{-4} | 37.82 | 3.09×10^{-4} | 0.91 | 3.58×10^{-1} |
| Proposed | 5.52×10^{-3} | N/A | 45.21 | N/A | 0.94 | N/A |
| IW (N=21) | | | | | | |
| Original | 4.61×10^{-1} | 2.98×10^{-5} | 13.15 | 2.98×10^{-5} | 0.32 | 2.98×10^{-5} |
| Method 1 [1] | 3.63×10^{-2} | 1.49×10^{-2} | 29.51 | 1.29×10^{-1} | 0.87 | 3.18×10^{-3} |
| Method 2 [9] | 3.11×10^{-2} | N/A | 30.50 | N/A | 0.90 | N/A |

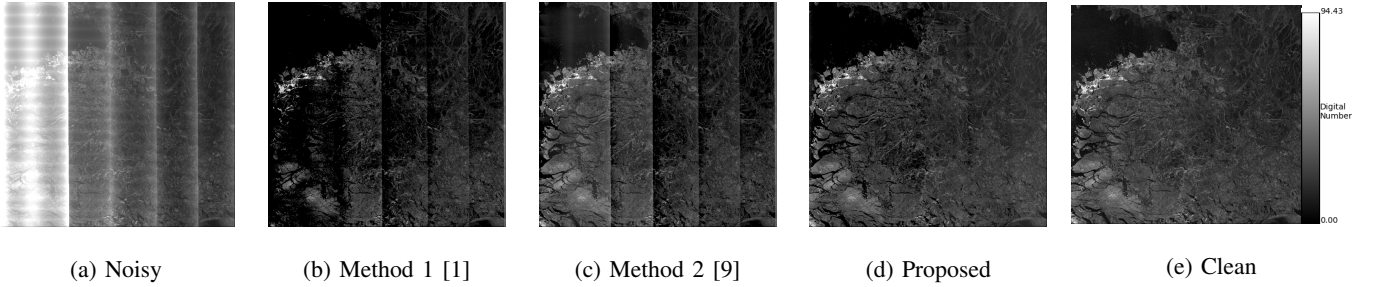


Fig. 7: Simulated EW correction comparison. Visually the proposed method is able to remove the sharp discontinuities between subswaths. a)SSIM=0.45,P-RNMSE= 3.5×10^{-1} ,PSNR=20.8 b) SSIM=0.73,P-RNMSE= 6.7×10^{-2} ,PSNR=28.2 c) SSIM=0.89,P-RNMSE= 1.8×10^{-2} ,PSNR=37.7 d) SSIM=0.91,P-RNMSE= 1.1×10^{-2} ,PSNR=39.4

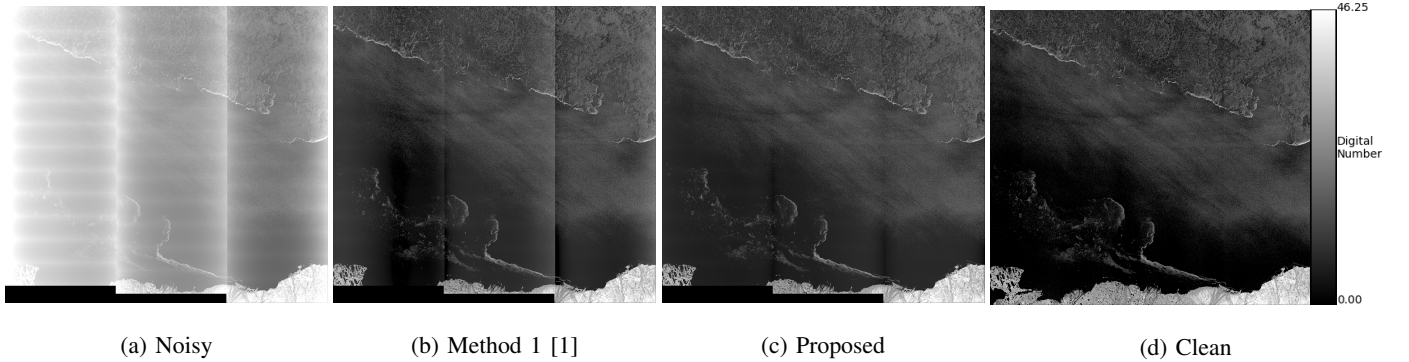


Fig. 8: Simulated IW correction comparison. The proposed method produces cleaner results, albeit still with some distortion at the subswath boundaries. Again, note that no comparison was made to the Method 2 [9] due to it not being implemented for IW images. a)SSIM=0.23,P-RNMSE= 2.5×10^{-2} ,PSNR=32.0 b) SSIM=0.85,P-RNMSE= 3.6×10^{-3} ,PSNR=48.8 c) SSIM=0.90,P-RNMSE= 3.4×10^{-3} ,PSNR=49.4

intensity varies in subswaths for between the proposed and Method 1 [1]. This is done by directly comparing the overall intensity in each subswath between the methods through paired differences.

The data used in this experiment is essentially the same as the previous experiment, but instead of attempting to measure the quality of the images, we measure overall change in bias. For each corrected image, the mean intensity measurements were computed for each subswath. Thus, a vector of size 40 (EW) or 18 (IW) was made for each subswath and each of the two correction methods.

The change in bias was evaluated on a subswath-wise manner so that the paired differences were taken between the

two correction method for each subswath. The significance of its difference vector was evaluated using a two-tailed paired t-test, with the implied null hypothesis being that the mean intensity for the subswath is the same for the two methods. Ultimately, all intensities showed the means were significantly different, save for EW4, EW5, and IW1. These results are shown in Table III. Overall, this indicates that there is a significant difference in radiometric bias between the results of the two methods.

V. DISCUSSION

Within the experiments, there is significant evidence that the proposed method is able to accomplish the goal for

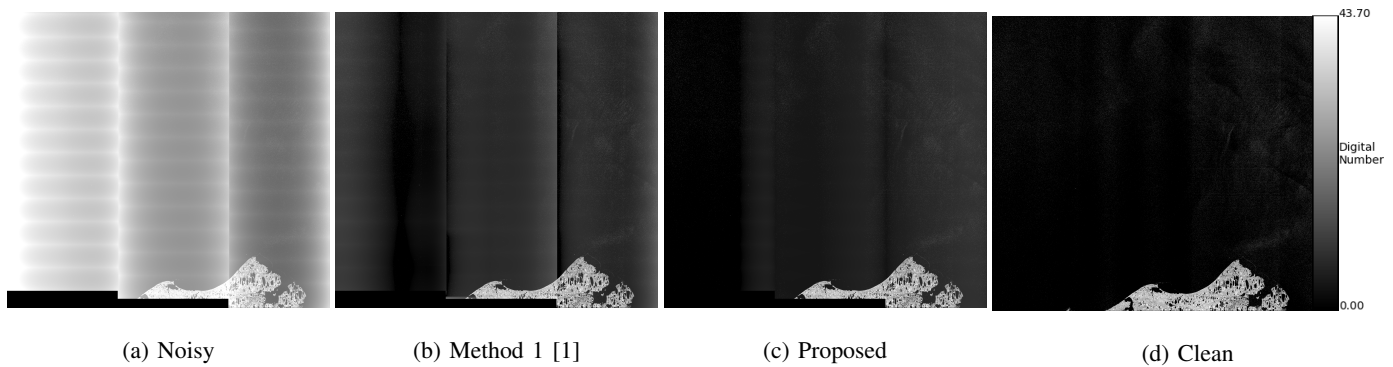


Fig. 9: Example of a scene generated from the simulation experiment where the proposed method is less successful. Although the transitions between subswaths are continuous, the first range split in IW1 is not estimated correctly and much of the image appears brighter than ground truth. a) SSIM=0.07,P-NRMSE= 4.6×10^{-1} ,PSNR=10.5 b) SSIM=0.48,P-NRMSE= 5.3×10^{-2} ,PSNR=27.4 c) SSIM=0.70,P-NRMSE= 4.6×10^{-2} ,PSNR=27.0

TABLE II: Experiment comparison for range regression over open water. The median R-NMSE results are reported for the samples for both EW (N=40) and IW (N=18) images. The listed p-value is derived through a one-tailed Wilcoxon test to determine if the proposed method has a lower R-NMSE than the other methods.

| Method | Median R-NMSE | P-value |
|--------------|-----------------------|-------------------------|
| EW (N=40) | | |
| Original | 2.87×10^2 | 1.78×10^{-8} ✓ |
| Method 1 [1] | 3.75×10^0 | 5.92×10^{-8} ✓ |
| Method 2 [9] | 3.20×10^0 | 1.88×10^{-6} ✓ |
| Proposed | 1.07×10^0 | N/A |
| IW (N=18) | | |
| Original | 2.04×10^1 | 9.82×10^{-5} ✓ |
| Method 1 [1] | 9.10×10^{-1} | 3.21×10^{-2} ✓ |
| Proposed | 3.83×10^{-1} | N/A |

TABLE III: Average intensity values of different subswaths for Method 1 [1] and proposed. The percentage of the original measurement is also recorded below for reference. P-values from paired two-tailed t-test are recorded comparing the distribution of intensities between Method 1 and proposed. For reference, the percentage is reported under the values to indicate the average ratio of the final intensity with respect to the original unprocessed measurements (i.e., the noisy image).

| Subswath | Method 1 [1] | Proposed | P-value (t-test) |
|----------|--------------|----------|-------------------------|
| EW1 | 862 | 1124 | 4.36×10^{-2} ✓ |
| | 8.74% | 11.39% | |
| EW2 | 988 | 1166 | 3.69×10^{-4} ✓ |
| | 27.50% | 32.46% | |
| EW3 | 1006 | 1127 | 1.32×10^{-3} ✓ |
| | 34.01% | 38.12% | |
| EW4 | 1123 | 1074 | 3.72×10^{-1} ✗ |
| | 50.37% | 48.15% | |
| EW5 | 1049 | 968 | 3.41×10^{-1} ✗ |
| | 52.82% | 48.78% | |
| IW1 | 455 | 441 | 4.67×10^{-1} ✗ |
| | 26.36% | 25.51% | |
| IW2 | 216 | 192 | 1.17×10^{-2} ✓ |
| | 24.04% | 21.33% | |
| IW3 | 297 | 256 | 1.10×10^{-3} ✓ |
| | 41.15% | 35.45% | |

compensating for non-linear mis-shape in the noise floor. The first two experiments directly support the ability of the proposed method to improve image quality. While the third experiment indicates that there is a significant difference in radiometric calibration, we describe the implications of this in more detail below. We also discuss some other important details regarding parameter estimation and other factors on the observed intensity.

The results from the simulation experiment also indicate that the proposed method is able to result in a better quality images than the alternatives under the assumptions of the simulation pipeline. The three metrics generally support the effectiveness of the proposed method over the baseline methods. Statistically, the metrics showed significant improvement except for the PSNR metric in EW and the SSIM metric in IW. There were some examples however, as shown in Fig. 9, where the proposed method was less successful. This highlights a key assumption made by the proposed method of there being sufficient critical points along the line $mp + b$ that best fits the true noise floor. If there are an insufficient number of points, then the parameters may estimate in a less successful manner, which typically occurs when m is tightly fit to the constraints of $m \geq -0.75$ or $m \leq -1.25$. For example in Fig. 9, $m = -1.25$ for the rightmost range split of IW1, where the result is most divergent from the ground truth.

The images generated in the second experiment such as in Figures 10 and 11 show that the proposed method is able to compensate for the noise floor in both EW and IW images. Visually, there was a large improvement in image quality induced by the proposed method over the other methods, which was particularly evident by the smooth transitions between subswaths. To this end, this demonstrates visual evidence that the non-linear misfit is compensated effectively. Quantitatively, the range regression over open water provides strong evidence that the proposed method can estimate more accurate noise floors than the alternative methods. The proposed method had significant improvement of normalized mean squared error with respect to the regression along the range. Specifically for EW images, the improvement is of high impact and is successful in normalizing the intensity changes. For IW

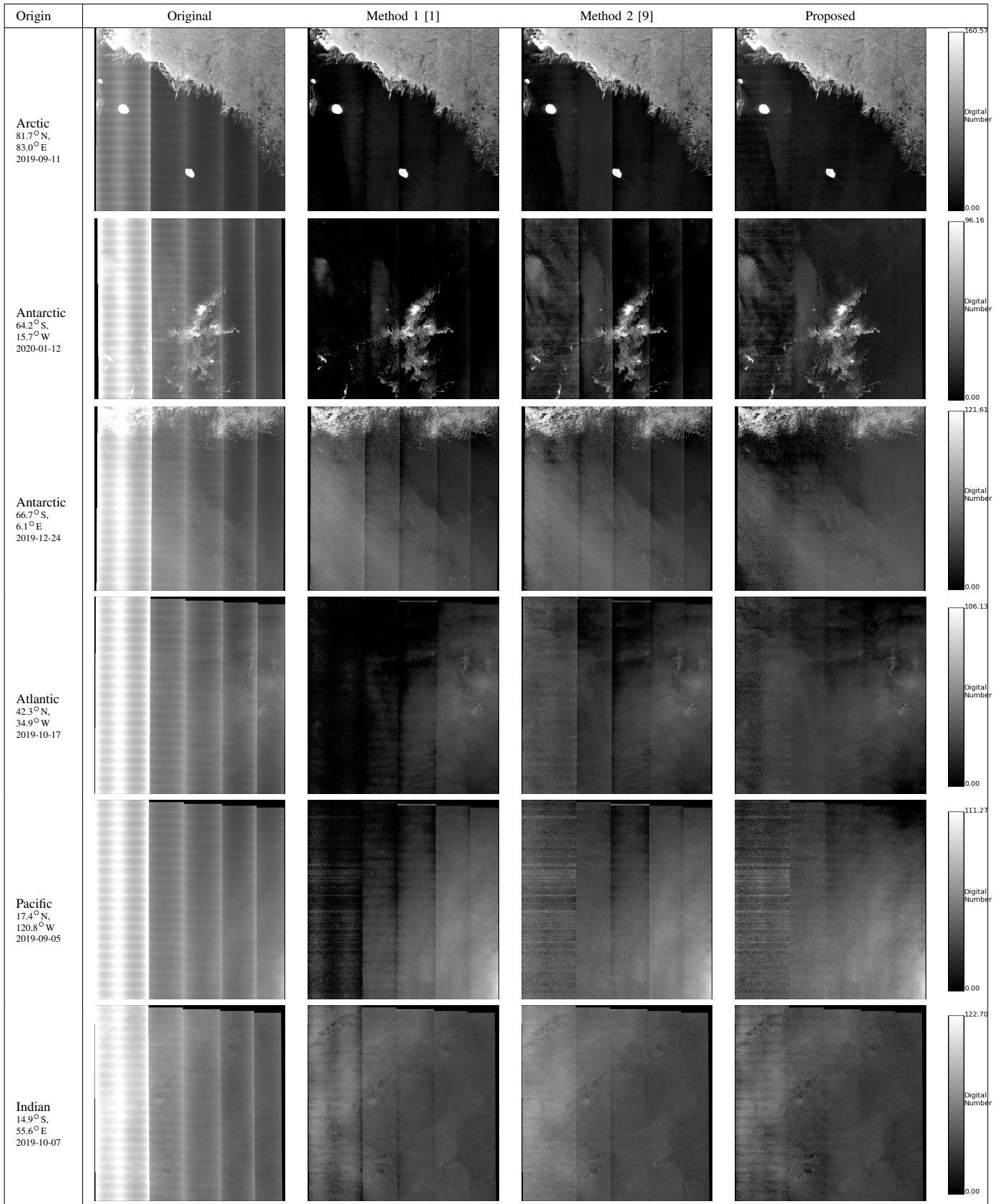


Fig. 10: Comparison of Sentinel-1 EW images. Coordinates coorespond to the center.

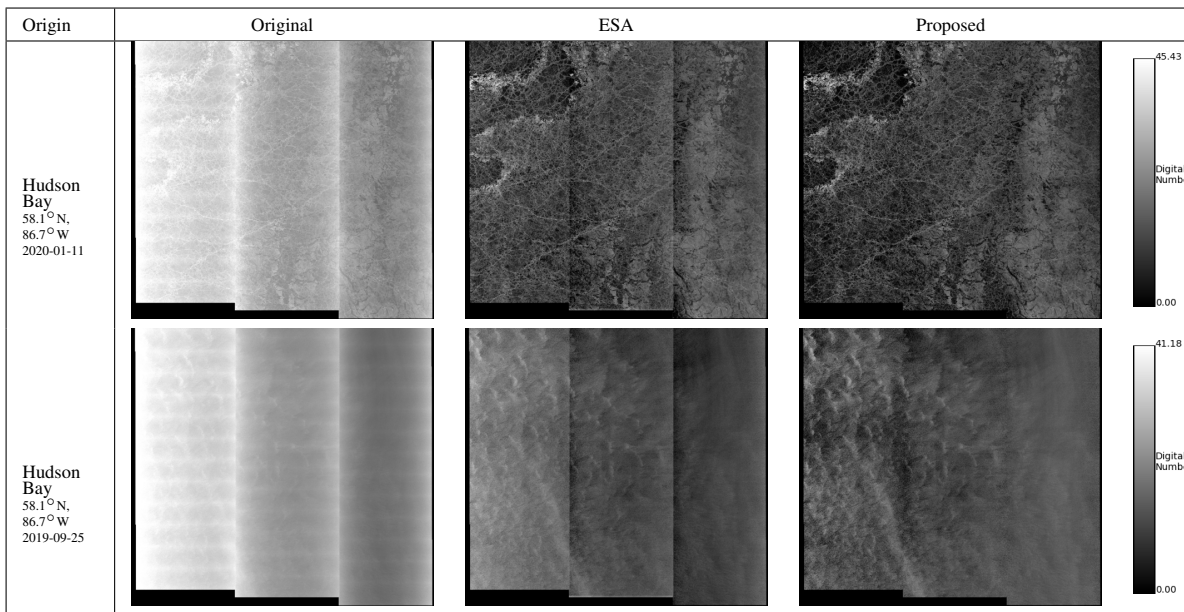


Fig. 11: Comparison of Sentinel-1 IW images captured within the Hudson Bay.

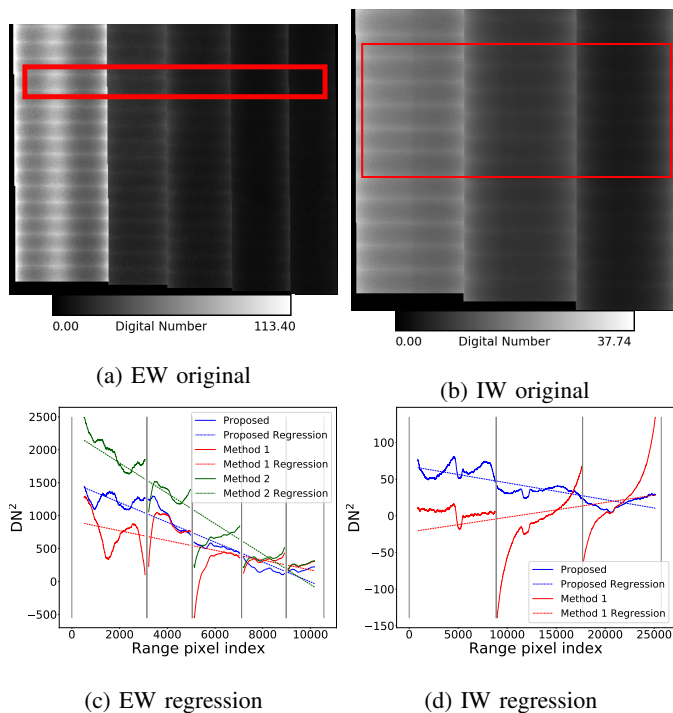


Fig. 12: Top figures show zones of open water that are pre-selected in red. Bottom figures showing the regression along the range over sections of open water. The proposed method (blue), is compared to the Method 1 [1] (red) and Method 2 [9] (green). In these examples, Methods 1 and 2 have noticeable discontinuities at the start and end of each subswath, something that the proposed method is able to compensate.

images, there was still significant improvement, albeit with less impact due to the higher signal-to-noise floor-ratios from the sensor mode. In terms of the types of surfaces captured in IW images, noise floor compensation towards land surfaces is less necessary since the measurements are dominated by backscatter intensity. Instead, the method shows more promise towards IW images containing water or ice, and thus could be useful towards supporting remote sensing applications over inland water or ice. Although our study was mainly focused towards Sentinel-1 images of IPF version 3.1 or above, our method is still applicable versions below that, so long as azimuth noise vectors are available. To verify we evaluated our method on a set of 41 EW images from our previous study [9] and found that our method had a median R-NMSE value that was 3.2 lower than our previous method, with a Wilcoxon p-value of 0.012 thanks to its ability to correct for the noise floor effects.

The main result from the third experiment is that there is a difference in overall intensity between the proposed method and Method 1 [1]. This implies that there is a significant difference in radiometric bias; an important factor depending on the remote sensing application. Whether this is an adverse change in radiometric bias is not clear. For example, Fig. 13 shows that Method 1 results in sections of the ice formation being removed because the intensity values are below zero. Because the ice formation is visible in the proposed method, this provides evidence that the total power of Method 1 may not be ideal and removing the noise floor while accurately recovering the backscatter of the ground targets is a non-trivial problem. This problem could conceivably be alleviated if one has some prior knowledge of the correct measurements for some fiducials in the image. This information can be embedded into the proposed method in two ways. The first is through adjusting the choice of B in Algorithm 2. The second is by augmenting equation 6 with a regularization term on \mathbf{o}

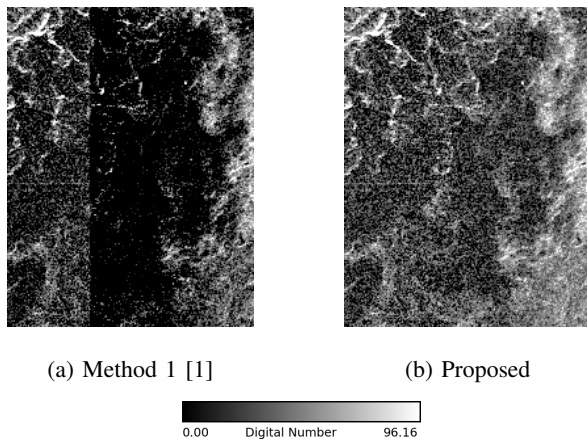


Fig. 13: Close up example comparing Method 1 [1] and proposed denoised examples extracted from the image in $64.2^{\circ}\text{S}, 15.7^{\circ}\text{W}$, 2020-01-12, as seen in Fig. 10. Notice that Method 1 loses ice features due to the noise floor being too high at the subswath transition.

to guide the estimates to towards the desired intensity values.

In terms of parameter estimation, Figs. 14a,14b summarize the parameters m , b , and o estimated for the Sentinel-1 experiment. An interesting observation is the correlation between m and b is extremely high, with coefficients of 0.9778 for EW and 0.9777 for IW. The plot shows that each parameter estimated is not independent, with each parameter having a clear centre. However, the spread of estimates is still quite large. Figs. 14c,14d likewise show the spread of parameters for the simulation experiment. The same correlation between m and b is clear, with coefficients of 0.9925 for EW and 0.9961 for IW. Compared to Figs. 14a,14b, the spread of the estimates in the simulation experiment is much smaller. Indeed for the simulation experiment the sum of standard deviations was 0.6962 for EW and 0.2388 for IW while for the Sentinel-1 experiment it was 1.077 for EW and 0.3787 for IW. This is an important observation that supports the importance of estimating new parameters for every scene because if the ideal parameters were the same for each scene the spread of both of the experiments would be more similar. Specifically for the simulation experiment, the parameter estimates appear to be centred around the ground truth for the EW case, especially in lower SNR subswaths (e.g., EW1), with estimates becoming more divergent with later subswaths with higher SNR (e.g., EW5). The estimates also showed divergence for the IW case in later subswaths. An explanation for the divergence may be due to the over-determined nature of the model. This is especially true for subswaths with a lower magnitude relative noise floor, where the curvature of P is less severe. Depending on the magnitude and shape of X and P , different combinations of parameters can result in similar results.

Another factor to consider is that the total intensity of individual bursts in a subswath can differ due to non-local targets. Fig. 15 shows two examples where the intensity from high backscatter targets bleeds over into low intensity targets within the burst, thereby causing discontinuity between

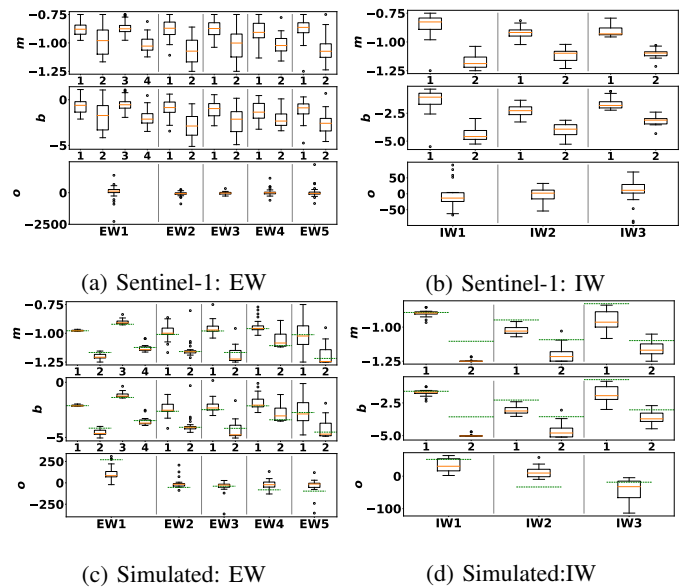


Fig. 14: Spread of parameter estimates for the experiment on Sentinel-1 images (a) and (b) and the simulated experiment (c) and (d) for m (top), b (middle), and o (bottom). The box plots are marked by their range split on the horizontal axis and divided into their respective subswaths by the gray vertical lines. The simulated experiment have the ground truth parameters used to generate the noise floor marked by the horizontal dashed green lines.

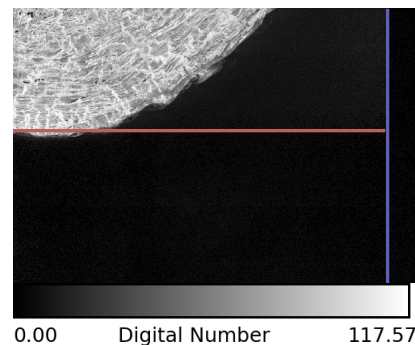


Fig. 15: Example of an IW image where high intensity targets bleed over into other targets within the burst. This causes discontinuity between adjacent bursts, as indicated by the burst division (red line). The division between subswaths (blue line) is identified for reference.

adjacent bursts. The cause for this likely lies in the signal processing pipeline, where the observed signal components of the backscatter radiation within the range of the subswath is transformed into the spatial intensity seen within the image. This cannot be compensated by the current proposed method because it assumes that the noise floor should be calibrated in the same way for each burst throughout the entire subswath. Correcting this on the image processing side would require estimating parameters for each specific burst. However, this would be difficult to accomplish due to the limited amount of data in a single burst needed to produce estimates.

A final consideration regarding image quality is the compensation for speckle. While directly out of scope for this manuscript, it is worth mentioning its impact on the images. Speckle in SAR is typically modelled with the Gamma distribution [24] and is described as multiplicative noise, where its variance increases with respect to the original signal. As a result, even when the noise floor is subtracted the increased variance remains in regions where the noise floor was higher. If one were to combine a despeckling approach with our method, they must bear in mind that the statistics of speckle are still linked to that of the original measurements.

VI. CONCLUSION

In this manuscript we proposed a new model for estimating the noise floor in Sentinel-1 GRD intensity images in order to account for non-linear misfit of the default noise floor estimation that other methods in the literature cannot compensate for. The model considers the noise floor to be an power function of the radiation pattern power. We observed that different trends occur at different sections of each subswath and therefore estimate multiple power functions per subswath. Through log transformation the problem of estimating parameters for the power functions is relaxed to a linear programming problem. To account for affine imbalance between subswaths, subswath-wise offsets are computed using a weighted least squares approach, making the entire estimation a convex optimization problem. The method was overall successful in estimating the noise floor in both Sentinel-1 images and simulated images. While there is a change in radiometric bias, compared to the baseline method provided by the ESA, the impact of this will depend on the remote sensing application. While the focus of this work has been on maritime regions, the applicability of the method towards the heterogeneous features of land dominant scenes has not been evaluated. While the noise floor for land areas is less of a concern due to the higher signal to noise ratio, noise reduction on such scenes is nevertheless a topic for future study.

REFERENCES

- [1] Sentinel-1 Quality Control, "Sentinel-1 QC | IPF versions," June 2020.
- [2] D.-B. Hong and C.-S. Yang, "Automatic discrimination approach of sea ice in the Arctic Ocean using Sentinel-1 extra wide swath dual-polarized SAR data," *International Journal of Remote Sensing*, vol. 39, no. 13, pp. 4469–4483, 2018. [Online]. Available: <https://doi.org/10.1080/01431161.2017.1415486>
- [3] J. Karvonen, "Baltic Sea ice concentration estimation using Sentinel-1 SAR and AMSR2 microwave radiometer data," *IEEE Transactions on Geoscience and Remote Sensing*, vol. 55, no. 5, pp. 2871–2883, May 2017.
- [4] J.-W. Park, A. A. Korosov, M. Babiker, S. Sandven, and J.-S. Won, "Efficient thermal noise removal for Sentinel-1 TOPSAR cross-polarization channel," *IEEE Transactions on Geoscience and Remote Sensing*, vol. 56, no. 3, pp. 1555–1565, 2018.
- [5] W. Tan, J. Li, L. Xu, and M. A. Chapman, "Semiautomated segmentation of Sentinel-1 SAR imagery for mapping sea ice in Labrador Coast," *IEEE Journal of Selected Topics in Applied Earth Observations and Remote Sensing*, vol. 11, no. 5, pp. 1419–1432, May 2018.
- [6] K. Schmidt, M. Schwerdt, N. Miranda, and J. Reimann, "Radiometric comparison within the Sentinel-1 SAR constellation over a wide backscatter range," *Remote Sensing*, vol. 12, no. 5, March 2020.
- [7] Y. Gao, C. Guan, J. Sun, and L. Xie, "A wind speed retrieval model for Sentinel-1A EW mode cross-polarization images," *Remote Sensing*, vol. 11, no. 2, p. 153, January 2019.
- [8] F. M. Monaldo, C. Jackson, and X. Li, "On the use of Sentinel-1 cross-polarization imagery for wind speed retrieval," in *2017 IEEE International Geoscience and Remote Sensing Symposium (IGARSS)*, 2017, pp. 392–395.
- [9] P. Q. Lee, L. Xu, and D. A. Clausi, "Sentinel-1 additive noise removal from cross-polarization extra-wide TOPSAR with dynamic least-squares," *Remote Sensing of Environment*, vol. 248, p. 111982, October 2020. [Online]. Available: <http://www.sciencedirect.com/science/article/pii/S0034425720303527>
- [10] Y. Sun and X.-M. Li, "Denoising sentinel-1 extra-wide mode cross-polarization images over sea ice," *IEEE Transactions on Geoscience and Remote Sensing*, vol. 59, no. 3, pp. 2116–2131, 2021.
- [11] J.-W. Park, J.-S. Won, A. A. Korosov, M. Babiker, and N. Miranda, "Textural noise correction for sentinel-1 topsar cross-polarization channel images," *IEEE Transactions on Geoscience and Remote Sensing*, vol. 57, no. 6, pp. 4040–4049, 2019.
- [12] P. Q. Lee, L. Xu, and D. A. Clausi, "Recalibrating sentinel-1 additive noise-gain with linear programming." Waikoloa, Hawaii, USA: IEEE International Geoscience & Remote Sensing Symposium, July 2020, pending Print.
- [13] R. Piantanida, "Sentinel-1 level 1 detailed algorithm definition," Tech. Rep., 2019, retrieved June 23, 2020. <https://sentinel.esa.int/documents/247904/1877131/Sentinel-1-Level-1-Detailed-Algorithm-Definition>.
- [14] S. V. Hum, "Radio and microwave wireless systems," 2018, retrieved June 23, 2020. <http://www.waves.utoronto.ca/prof/svhum/ece422/notes/21-noise.pdf>.
- [15] L. Wang, K. A. Scott, D. A. Clausi, and Y. Xu, "Ice concentration estimation in the Gulf of St. Lawrence using fully convolutional neural network," in *2017 IEEE International Geoscience and Remote Sensing Symposium (IGARSS)*, 2017, pp. 4991–4994.
- [16] J. Wei and H. Chen, "Effect of roll angle error on spaceborne ScanSAR radiometric calibration in range," in *2007 International Symposium on Microwave, Antenna, Propagation and EMC Technologies for Wireless Communications*. IEEE, Aug 2007, pp. 1471–1475.
- [17] F. D. Zan and A. M. Guarnieri, "TOPSAR: Terrain observation by progressive scans," *IEEE Transactions on Geoscience and Remote Sensing*, vol. 44, no. 9, pp. 2352–2360, September 2006.
- [18] R. J. Duffin, "Linearizing geometric programs," *SIAM Review*, vol. 12, no. 2, pp. 211–227, 1970. [Online]. Available: <http://www.jstor.org/stable/2029221>
- [19] S. Boyd and L. Vandenberghe, *Convex Optimization*. Cambridge University Press, 2004, pp. 1–15.
- [20] A. Agrawal, R. Verschuere, S. Diamond, and S. Boyd, "A rewriting system for convex optimization problems," *Journal of Control and Decision*, vol. 5, no. 1, pp. 42–60, 2018.
- [21] S. Diamond and S. Boyd, "CVXPY: A Python-embedded modeling language for convex optimization," *Journal of Machine Learning Research*, vol. 17, no. 83, pp. 1–5, 2016.
- [22] B. O'Donoghue, E. Chu, N. Parikh, and S. Boyd, "Conic optimization via operator splitting and homogeneous self-dual embedding," *Journal of Optimization Theory and Applications*, vol. 169, no. 3, pp. 1042–1068, June 2016. [Online]. Available: <http://stanford.edu/~boyd/papers/scs.html>
- [23] —, "SCS: Splitting conic solver, version 2.1.2," <https://github.com/cvxgrp/scs>, Nov. 2019.
- [24] F. Argenti, A. Lapini, T. Bianchi, and L. Alparone, "A tutorial on speckle reduction in synthetic aperture radar images," *IEEE Geoscience and Remote Sensing Magazine*, vol. 1, no. 3, pp. 6–35, 2013.
- [25] D. Zwillinger, *CRC Standard Mathematical Tables and Formulae*, 31st ed. Chapman & Hall/CRF, 2003.
- [26] Z. Wang, A. C. Bovik, H. R. Sheikh, E. P. Simoncelli *et al.*, "Image quality assessment: From error visibility to structural similarity," *IEEE Transactions on Image Processing*, vol. 13, no. 4, pp. 600–612, 2004.



Peter Q. Lee received a B.C.S. (Hons.) in computer science at Dalhousie University in 2018, Halifax, NS, Canada, and a M.A.Sc. in Systems Design Engineering from the University of Waterloo in 2020, Waterloo, ON, Canada. He is currently pursuing a Ph.D at the University of Waterloo in Systems Design Engineering.

His research interests include topics in computer vision, machine learning, image processing, and more recently, robotics and optimal control.



Linlin Xu received the B.Eng. and M.Sc. degrees in geomatics engineering from the China University of Geosciences, Beijing, China, in 2007 and 2010, respectively, and the Ph.D. degree in geography from the Department of Geography and Environmental Management, University of Waterloo, Waterloo, ON, Canada, in 2014.

He is a Research Assistant Professor with the Department of Systems Design Engineering, University of Waterloo. He has published various papers on high-impact remote sensing journals and conferences. His research interests include hyperspectral and synthetic aperture radar data processing and their applications in various environmental applications.



David A. Clausi earned his Ph.D. (1996) in Systems Design Engineering at the University of Waterloo (Waterloo, Ontario, Canada). Afterwards, he worked in medical imaging at Mitra Imaging (Waterloo). He started his academic career in 1997 as an Assistant Professor in Geomatics Engineering at the University of Calgary, Canada. In 1999, Dr. Clausi returned to University of Waterloo and is now a Professor who specializes in the field of Intelligent Systems and is the Associate Dean Research & External Partnerships in the Faculty of Engineering.

Prof. Clausi has numerous contributions, publishing refereed journal and conference papers primarily in remote sensing, computer vision, image processing, and algorithm design. He was the Co-chair of IAPR Technical Committee 7 – Remote Sensing (2004-2006). He has published extensively, received many scholarships, paper awards, research awards, teaching excellence awards and his efforts have led to successful commercial implementations, culminating in the creation and sale of a high tech company.